ITC 1/54
Information Technology and Control
Vol. 54 / No. 1/ 2025
pp. 234-253
DOI 10.5755/j01.itc.54.1.38163

High Quality Visual Communication Image Enhancement Based on Deconvolution Algorithm Regularization of Salient Edges and Average Curvature Model

Received 2024/07/23 | Accepted after revision 2024/11/22

**HOW TO CITE:** Tan, S., Dong, L., An, L. (2025). High Quality Visual Communication Image Enhancement Based on Deconvolution Algorithm Regularization of Salient Edges and Average Curvature Model. *Information Technology and Control*, 54(1), 234-253. https://doi.org/10.5755/j01.itc.54.1.38163

# High Quality Visual Communication Image Enhancement Based on Deconvolution Algorithm Regularization of Salient Edges and Average Curvature Model

**Shuo Tan**
Design Interactions, Beijing Jiaotong University, Weihai, Weihai, 264401, China

**Lingye Dong**
Department of Humanities and Social Sciences, Shijiazhuang Institute of Railway Technology, Shijiazhuang, 050041, China

**Limei An**
Fine Arts Department, Hebei Vocational Art College, Shijiazhuang, 050011, China

**Corresponding authors:** lingyedong0523@163.com

Current prior methods for image knowledge are difficult to generalize to fuzzy images in specific fields, dark channel priors still face issues such as ineffective fuzzy kernel estimation, high computational costs, low computational efficiency, and obvious defects in imaging details. In order to avoid the interference of subjective and objective factors on image details and information quality, and to achieve image denoising, a deconvolution algorithm combining salient edges and average curvature (AC) regularization is proposed to achieve image deblurring processing. Firstly, the DARSE-AC algorithm combining salient edges and filtering regularization is proposed to improve image blur. Secondly, explicit and implicit strategy is used to solve image defects, and filtering processing is carried out based on considering the minimum surface and fast Fourier transform. The

proposed method was tested. The results showed that the success rate of image denoising was higher than other comparison algorithms. The repair results showed that the method effectively achieved deblurring. This optimization method had good convergence during the iteration process, with peak signal-to-noise ratio, structural similarity index measurement value, and error ratio of 31.03, 0.96, and 1.61, respectively. The algorithm that considers edge information and curvature regularization processing can better preserve the quality and details of image information, which can effectively provide new technical means and tools for visual communication.

KEYWORDS: Salient edges, AC regularization, Peak signal-to-noise ratio, Structural similarity index, Noise.

## 1. Introduction

As the visual foundation for human perception of the world, images are an important means for humans to obtain, express, and transmit information. Due to limitations in imaging equipment and external factors, the collected images are inevitably affected by noise, blurring, low resolution, and even contain some missing information, resulting in image distortion [10, 35]. Image degradation can hinder its analysis and use. Therefore, image restoration techniques should be used to restore the original clear image from degraded images to further improve the effectiveness and accuracy of subsequent image processing [19]. Traditional image restoration techniques typically utilize image filtering. However, the actual image details and noise have aliasing in the frequency band. This method is difficult to protect image edges while smoothing out noise. However, the subsequent application of diffusion methods based on partial differential equations also suffers from process instability and slow convergence [2]. The latest technology currently utilizes variational methods based on prior knowledge to achieve image restoration. This method can protect the edge details of the image while removing image blur, thereby achieving high-quality visual communication effects [27]. However, at present, it is difficult to generalize the prior knowledge of images to fuzzy images in specific fields. There still exist problems in the dark channel prior, such as ineffective estimation of fuzzy kernels, high computational cost, and low computational efficiency. The method using salient edges also has high computational complexity. The computational cost refers to the operations and iterative calculations involved in the minimum value filtering of the entire image, which can also indirectly reflect the computational burden. Computational efficiency refers to the efficiency of pixel data in computation and calculation, while computational complexity refers to the sequence of steps in image detection, including operator detection, image gradient calculation, threshold processing, edge extraction, and scale analysis. Therefore, a Deconvolution Algorithm based on Regularization of Salient Edges and Average Curvature (DARSE-AC) is proposed by combining the regularization of Average Curvature (AC) with salient edges. Its purpose is to improve the actual deblurring effect of images in high-quality visual communication and broaden its application scope in the computer vision and digital images.

High quality image formation is crucial for visual inspection and industrial production technology. However, due to factors such as light, shooting angle, and occlusion during the imaging process, there are significant defects in the imaging details of the image. The main contributions of this study are as follows. Firstly, when processing image estimation, the average curvature regularization is combined with gradient and edge highlighting for image fusion. Secondly, explicit and implicit prominent edge selection combined with AC regularization optimizes the blind deconvolution algorithm and constructs a new DARSE-AC convolution algorithm. Thirdly, a mixed segmentation strategy with auxiliary variables is introduced to solve the algorithm equation, and an average curvature filter is used to calculate the function equation. Then, the Fourier transform is applied to obtain the closed form solution of the Equation (4). The mutual inductance image filtering method estimates the fuzzy kernel in the equation and normalizes the calculated fuzzy kernel to improve image quality and perform denoising processing. The main focus of this article is image deblurring. To address the high computational cost and poor image quality, the research conducts on regularization and deconvolution algorithms for highlighting edges and average curvature. The research results of the Peak Signal-to-Noise Ratio (PSNR), Structural Similarity Index Measurement (SSIM), and Error Ratio

(ER) of the image under this method were obtained, with values of 31.03, 0.96, and 1.61, respectively, greatly preserving information quality and details. Through the above improvement ideas, it can be ensured that the theme of high-quality visual images can be presented in a more comprehensive and clear manner.

This study mainly elaborates on the manuscript content from five parts. The second part reviews relevant literature on image deblurring processing. The research has found that limited computational efficiency and high dependence on external data make it difficult for existing algorithms to achieve satisfactory results while ensuring algorithm performance. Therefore, in the third part of the study, the DARSE-AC is proposed to achieve image deblurring. The theory of average curvature regularization is introduced to achieve image processing. A new deconvolution algorithm is adopted to model the fused image, and a mixed segmentation strategy is used to solve the equation system for variable solving, ultimately improving image quality. The fourth part tests the method and image datasets by establishing an experimental environment and deep learning framework. The last part summarizes and discusses the entire text, and explains the shortcomings.

## 2. Related Works

The development of deep learning technology has led to the widespread application of image deblurring methods based on salient edges and AC [12]. Liu et al. [20] proposed a fast blind image deblurring algorithm based on salient edges and gradient cepstral, which effectively shortened the running time of traditional deblurring architectures. Xu et al. [34] proposed a knowledge enhanced adaptive deblurring algorithm based on salient edges and deep learning, which not only improved the global image deblurring effect, but also optimized the details of image edges. Yogananda et al. [37] proposed a multi-objective crawling search algorithm based on data edges to address image blur and high noise caused by object motion in actual scenes. This algorithm effectively improved the performance of image deblurring while removing noisy pixels. In response to the image blurring caused by atmospheric distortion in the original scene, Priya et al. proposed an image optimization algorithm using ant cuckoo search based on exponential and salient edges. This not only improved the accuracy and robustness of image deblurring, but also strengthened its adaptability [24]. Regarding the image blur in dynamic scenes, Zhang et al. [38] proposed a new deblurring algorithm based on recursive neural networks with salient edges and multi-scale spatial variations, which effectively improved the accuracy and efficiency of image deblurring.

In addition, to address the issues related to high-order derivatives in image deblurring, Fairag et al. [7] proposed a two-level model for image denoising based on AC regularization, effectively improving the performance of image deblurring while eliminating the staircase effect. In response to the image deblurring in image processing tasks, Wang et al. [30] proposed a scalar auxiliary variable scheme based on AC regularization, which effectively enhanced the robustness of the method while improving the image deblurring effect. To address the related issues of the Euler elastic energy model in handling image blurring, Liu et al. [17] proposed a fast image deblurring algorithm based on minimizing elastic properties and AC regularization, which effectively enhanced the robustness of image deblurring. Xie et al. [33] constructed a prior guided variational architecture for the red channel based on a complete underwater imaging model and AC regularization, effectively improving the deblurring performance of underwater images. Zhou et al. [15] normalized the nodes of graph convolutional network architecture to improve the model smoothness relative to input node features. The experiment showed that this method had good applicability and generalizability. Regarding the image quality in mobile imaging, Gampala et al. [9] combined deep learning algorithms with deblurring loops to improve image restoration quality. Fatichah et al. [8] used deep multi-scale CNN networks and end-to-end generative adversarial network algorithms to achieve image deblurring. The results showed that this deep learning method performed well in structural similarity indicators, which could effectively improve image clarity. Wu et al. [32] proposed a deep convolutional neural network for blind image quality indicators, which was designed to jointly optimize multi-level feature extraction in an end-to-end framework while considering hierarchical degradation. The results indicated that this method had good superiority compared with benchmark data. Its parameters were implemented in micro-processing systems.

From domestic and foreign research, current image deblurring methods still suffer from high computational costs and low computational efficiency. The method proposed based on salient edges has high computational complexity and high dependence on external related data. Therefore, the DARSE-AC algorithm combining salient edges and AC regularization innovatively utilizes mutually guided image filters. Explicit edge selection is performed when using AC regularization to hide unfavorable structures. Meanwhile, the AC regularization of L0 norm fused with gradients effectively optimizes the model.

## 3. Deconvolution Algorithm Combining Salient Edges and Mean Curvature Regularization

The current deconvolution algorithm has many shortcomings. Therefore, this section optimizes the blind deconvolution algorithm through explicit and implicit salient edge selection, combined with AC regularization. It mainly achieves explicit edge selection based on mutually guided image filtering, while using AC regularization to eliminate unfavorable architectures.

### 3.1. Salient Edges and Mean Curvature Regularization Theoretical Analysis

At present, in the actual imaging process under visual communication, many factors lead to image blurring and high noise. As the grayscale change rate increases, boundaries are more likely to become boundary edges. When the edge has a clear boundary, it can be called an explicit convex edge type. The edge type that can only be obtained through computer boundary detection is called an implicit convex edge [28]. Figure 1 shows a comparison of image, contour, first derivative, and second derivative in salient edge detection.

From Figure 1, salient edge detection of images can be roughly divided into four types, named a, b, c, and d respectively in the study. The position where the edge appears is the boundary point between two parts in the image, which can be represented and described by the derivative of the function change rate. Edge points usually appear in the part where the first derivative reaches its maximum value or the second derivative reaches zero. Type A and Type B are similar, with edge points always appearing at the zero point of the positive negative transition. The situation of C-type and D-type is similar. After reaching a certain value, the trend of C-type remains unchanged. The D-type first rises until a platform is formed, and then falls back.

The second-order derivative method of edge detection is prone to being overly sensitive to noise, even though higher-order derivatives can be used to find edges in principle. The salient edge detection method mainly considers the presence of blur kernels, which requires removing detailed information of hidden images during the iterative process [21, 13]. Regularization is a method of adding additional information to a model to prevent over-fitting and help improve model performance. The selection of regularization parameters in the cost function of image deconvolu-

**Figure 1**
Comparison results of prominent edge detection

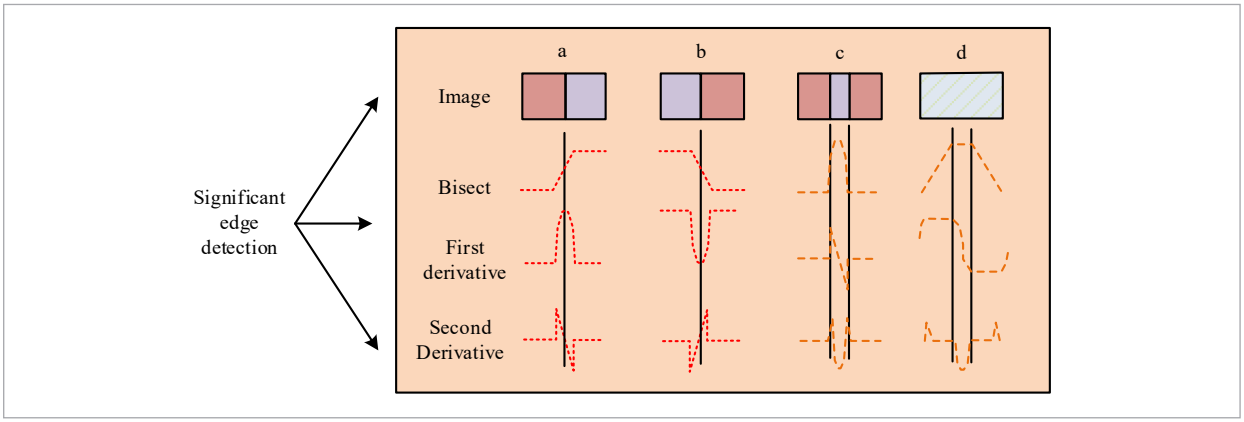

tion involves empirical adjustment, and its accuracy is difficult to guarantee. Therefore, Rajora et al. [25] proposed an image deconvolution framework based on average gradient descent, which can effectively perform uniform deconvolution on data with different levels of noise. The traditional regularization term for solving image problems relies on partial derivatives, while optimizing the average curvature to partition the image into extremely small surfaces can effectively handle this set until the model reaches convergence. Therefore, a blind convolution method combining implicit convex edge selection with explicit convex edge selection is proposed. Generally speaking, most implicit salient edge selection methods are similar to the calculation methods of latent clear images and blur kernels in image deblurring frameworks, as shown in Equation (1).

$$\begin{cases} I = \arg\min_{I} \Theta\left(A - I \otimes k\right) + \gamma_1 \psi_1\left(I\right) \\ k = \arg\min_{k} \Theta\left(A - I \otimes k\right) + \gamma_2 \psi_2\left(k\right) \end{cases}. \tag{1}$$

In Equation (1), $I$ represents a potentially clear image. $A$ represents the actual observed blurred image. $\gamma_1$ and $\gamma_2$ represent regularization terms. $\psi_1$ and $\psi_2$ represent corresponding non-negative parameters. $k$ represents a fuzzy kernel. $\Theta(\cdot)$ represents the data fitting function. The explicit salient edge method obtains the calculated correlation expression, as shown in Equation (2).

$$\begin{cases} \min_{I} \Theta\left(A - I \otimes k\right) + \varpi_z \left\|\nabla I - \nabla z\right\|_2^2 + \gamma_1 \psi_1\left(I\right) \\ \min_{k} \Theta\left(\nabla A - \nabla z \otimes k\right) + \gamma_2 \psi_2\left(k\right) \end{cases}. \tag{2}$$

In Equation (2), $\varpi_z$ represents a non-negative parameter. $z$ represents the main structure of the potentially clear image $I$. $\nabla$ represents the gradient operator. Overall, there are issues with the selection of $\psi_1\left(I\right)$ and $\nabla z$ when using salient edges. The former is usually carefully designed in implicit salient edge methods. However, it is easily overlooked in explicit salient edge methods. Therefore, the explicit and implicit edge selection strategies proposed in the study are beneficial for fuzzy kernels to estimate more reliable edges. In addition, they continuously approximate segmented minimal surfaces through AC regularization. For the latter calculation, the impulse filtering operation is not applied in $z$. Previous high-order regularization models can overcome the staircase effect while preserving the main structure of the image. However, due to the lack of critical geometric prior information, some important geometric features of the image cannot be preserved. Therefore, AC is proposed as a constraint regularization term for image surface processing, which is first introduced as an AC driven diffusion method into noise removal. Based on this, an AC minimization model for image denoising is constructed, which is expressed as Equation (3).

$$\min_{v \in L^2(\Omega)} \int_{\Omega} \left| \nabla \cdot \frac{\nabla v}{\sqrt{1 + \left|\nabla v\right|^2}} \right| dx + \frac{\varphi}{2} \int_{\Omega} \left(v - e\right)^2 dx \,. \tag{3}$$

In Equation (3), $v$ represents a potentially clean image. $\Omega$ represents a bounded open set with continuous boundaries, i.e. the image domain. $L^2$ represents the L2 norm. $x$ represents the pixels belonging to $\Omega$. $\varphi$ represents the Lagrange multiplier related to constraints. $e$ represents the observation image defined on $\Omega$. The L1 norm of average curvature has been proven to be an ideal regularization method for image denoising. It not only preserves image contrast and sharp edges of objects, but also eliminates the staircase effect. Therefore, the AC regularization in this study is based on the regularization method and explicit method used in Equation (3). Then, it is combined with the L0 norm of gradients as $\psi_1\left(I\right)$. To understand this process, the relationship between AC and minimal surfaces needs to be analyzed. In the geometric architecture of actual image processing, grayscale image $I\left(p,q\right)$ is embedded into three-dimensional space to form a surface of the image. The AC expression of the image surface and its surface area definition are shown in Equation (4). This content is similar to the method proposed by Coeurjolly [5] to reconstruct the surface of digital images using variational methods. The regularization tool proposed by Coeurjolly [5] to process digital data can effectively provide technical means for material art modeling.

$$\begin{cases} \Re\left(\Im\right) = \left[\left(1 + I_q^2\right) I_{pq} - 2 I_p I_q I_{pq} + 1\left(1 + I_p^2\right) I I_{qq}\right] \Big/ \left[2\left(1 + I_p^2 + I_q^2\right)^{3/2}\right] \\ \mathbb{Z}\left(\Im\right) = \iint\limits_{(p,q)\in\Omega} \sqrt{1 + \left|\nabla I\right|^2}\, dpdq \end{cases}. \tag{4}$$

In Equation (4), $\Re\left(\Im\right)$ represents the AC regularization of the image surface $\Im$. $p$ and $q$ represent the horizontal and vertical coordinate points belonging

to the spatial coordinates of $\Omega$. $\mathbb{Z}(\Im)$ represents the surface area of the image surface $\Im$. When it is minimized, it can be called a minimum surface. In addition, when the area of the potential image is small, it is more conducive to estimating the blur kernel. At this point, the corresponding minimization problem can be constrained through the AC regularization expression of image $I$.

### 3.2. Deconvolutional Models and Image Estimation

A fuzzy kernel estimation deconvolution algorithm model is constructed based on salient edge and AC regularization theory. Significance detection and edge detection are based on the frequency of each part of the image in the time domain. Prior knowledge related to positional variables and constraining the solution space can obtain clear image restoration results [18]. Yin et al. applied the two-dimensional Hessian sparse deconvolution algorithm based on image processing technology to digital beamforming technology. The results showed that the improved method effectively improved the detection resolution of acoustic processing under low signal-to-noise ratio [36]. Considering the impact of noise interference on blind deconvolution algorithms and the drawbacks of manually mining images using regularized image priors, this study combines L0 norm AC regularization with fused gradients and convex edges to construct a new deconvolution algorithm model, namely the DARSE-AC algorithm model. The deconvolution model can restore clear images through iterative operations. The corresponding calculation expression is shown in Equation (5).

$$\begin{cases} \min\limits_{I} \|I \otimes k - A\|_2^2 + \lambda \|\nabla I - \nabla z\|_2^2 + \xi \|\nabla I\|_0 + \theta \mathbb{Q}(I) \\ \min\limits_{k} \|\nabla z \otimes k - \nabla A\|_2^2 + \tau \|k\|_2^2 \end{cases}. \tag{5}$$

In Equation (5), $\lambda$, $\xi$, $\theta$, and $\tau$ represent penalty parameters. The estimation for image $I$ and blur kernel $k$ is particularly important. The actual regularization term of the gradient L0 norm is non-convex. Regularization, as one of the important contents in explaining high variance problems, is one of the methods to overcome over-fitting problems. Among them, Xu et al. [34] utilized the sparsity effect and denoising characteristics of sparse dictionaries to propose a norm-based sparse dictionary encoding regularization term for feature extraction of bi-adjacency graphs. The auxiliary function was constructed to generate solutions. The results show that this method can effectively achieve the separability of heterogeneous data and is robust to noise. Therefore, the study introduces auxiliary variables to replace $\nabla I$ and $I$ based on the semi-quadratic splitting strategy solution equation (i.e. Equation (5)). The optimized expression of the minimization problem is shown in Equation (6).

$$\min_{I,\alpha,\beta} \|I \otimes k - A\|_2^2 + \lambda \|\nabla I - \nabla z\|_2^2 + \xi \|\beta\|_0 + \theta \mathbb{Q}(\alpha) + \xi_1 \|\beta - \nabla I\|_2^2 + \theta_1 \|\alpha - I\|_2^2. \tag{6}$$

In Equation (6), $\xi_1$ and $\theta_1$ represent non-negative penalty parameters. $\alpha$ and $\beta$ represent two auxiliary variables. When the non-negative penalty is sufficiently large, the solution in Equation (6) is equivalent to the solution obtained in Equation (5). Therefore, the study solves Equation (6) by alternately optimizing the two auxiliary variables and $I$. When the $I$ value is given, the auxiliary variables $\alpha$ and $\beta$ are expressed, as shown in Equation (7).

$$\begin{cases} \min\limits_{\alpha} \theta \mathbb{Q}(\alpha) + \theta_1 \|\alpha - I\|_2^2 \\ \min\limits_{\beta} \xi \|\beta\|_0 + \xi_1 \|\beta - \nabla I\|_2^2 \end{cases}. \tag{7}$$

In Equation (7), the second row of equations is essentially a minimizing pixel problem. The existing gradient descent algorithms have low computational efficiency, high dependence on display computation AC, and complex derivation formats. Therefore, in order to avoid this problem, the AC filter is introduced in the study to address it. The main idea is to minimize AC regularization. Bernstein's theorem states that applying AC regularization is equivalent to assuming that the signal is piece-wise linear, which can minimize the piece-wise linearization method for linear functions. The numerical approximation of AC can be obtained through simple convolution operations, as shown in Equation (8).

$$\Re(I) \approx \begin{bmatrix} -1/16 & 5/16 & -1/16 \\ 5/16 & -1 & 5/16 \\ -1/16 & 5/16 & -1/16 \end{bmatrix} \otimes I. \tag{8}$$

In Equation (8), $\Re(I)$ represents the AC regularization of the image surface $I$. Therefore, for the minimization problem of AC, the AC filter first performs operations on the kernel of Equation (8) in four half

edge windows, namely the projection distance. Next, a value with the minimum absolute projection distance is selected to update the central pixel. To ensure that the total energy in the solution equation for the first row $\alpha$ of Equation (6) does not increase, corresponding additional condition is introduced. It is expressed as Equation (9).

$$\theta_1\left(\left\|\alpha_m - I\right\|_2^2 - \left\|\alpha_{m+1} - I\right\|_2^2\right) < \theta\left(\mathbb{Q}\left(\alpha_{m+1}\right) - \mathbb{Q}\left(\alpha_\alpha\right)\right). \quad (9)$$

In Equation (9), $m$ represents the number of pixels. When $\alpha$ and $\beta$ are given, the solution expression for image $I$ is shown in Equation (10).

$$\min_I \left\|I \otimes k - A\right\|_2^2 + \lambda\left\|\nabla I - \nabla z\right\|_2^2 + \xi\left\|\beta - \nabla I\right\|_0 + \theta_1\left\|\alpha - I\right\|_2^2. \quad (10)$$

Equation (10) is a minimizing quadratic optimization problem. It can effectively obtain the closed form solution of $I$ using Fourier transform, as expressed in Equation (11).

$$\begin{cases} I = \Psi^{-1}\left(\overline{\Psi(k)} \circ \Psi(A) + \lambda Y_z + \xi_1 Y_\beta + \theta_1 \Psi(\alpha)\right) \Big/ \left(\overline{\Psi(k)} \circ \Psi(k) + (\lambda + \xi_1) Y_\nabla + \theta_1\right) \\ z = \overline{\Psi\left(\nabla_g\right)} \circ \Psi\left(\nabla_g z\right) + \overline{\Psi\left(\nabla_u\right)} \circ \Psi\left(\nabla_u z\right) \\ Y_\beta = \overline{\Psi\left(\nabla_g\right)} \circ \Psi\left(\alpha_g\right) + \overline{\Psi\left(\nabla_u\right)} \circ \Psi\left(\alpha_u\right) \\ Y_\nabla = \overline{\Psi\left(\nabla_g\right)} \circ \Psi\left(\nabla_g\right) + \overline{\Psi\left(\nabla_u\right)} \circ \Psi\left(\nabla_u\right) \end{cases}. \quad (11)$$

In Equation (11), $\Psi^{-1}(\cdot)$ represents the Fast Fourier Transform (FFT) operation. $\overline{\Psi(\bullet)}$ represents the complex conjugate operation. $\Psi(\cdot)$ represents the FFT operation. $Y$ represents the matrix composed of $\nabla_p$ complex conjugate operation and FFT operation, and the $\nabla_q$ complex conjugate operation and FFT operation. $\circ$ represents pixel multiplication. $\nabla_g$ represents the gradient in the horizontal direction. $\nabla_u$ represents the gradient in the vertical direction. In the estimation of fuzzy kernel $k$, after obtaining the actual image $I$, it is necessary to further extract the main structure $z$ from $I$ to better estimate the fuzzy kernel. The latest mutual guidance image filtering method is used to achieve this process. The reason is that there are no other reference images in the image. The study utilizes Fourier transform to solve the closed form solution of the equation, effectively optimizing the solving equation, which can reduce computational complexity to a certain extent. Meanwhile, due to the optimization of auxiliary variables and the introduction of additional conditions during filtering processing, the integrity of information data can be well ensured. Therefore, the self-guided mode in this method is applied to estimate the fuzzy kernel. The computational expression is shown in Equation (12).

$$\min_z \left\|z - I\right\|_2^2 + \varsigma'' \sum_{(p,q)} \sum_{c \in \{g,u\}} \frac{\left(\nabla_c z(p,q)\right)^2}{\left(\max\left(\left|\nabla_c z(p,q)\right|, \mu\right)\right)}. \quad (12)$$

In Equation (12), $\varsigma''$ represents a non-negative weight parameter. $u$ represents the auxiliary variable of the non-linear channel denominator. $c$ represents the number of color channels. $\mu$ represents a smaller non-negative constant to avoid divisor 0, which is 0.01. Therefore, the estimation method flow for image $I$ and blur kernel $k$ in the study is shown in Figure 2.

**Figure 2**

Schematic diagram of the estimation method flow for image $I$ and fuzzy kernel $k$

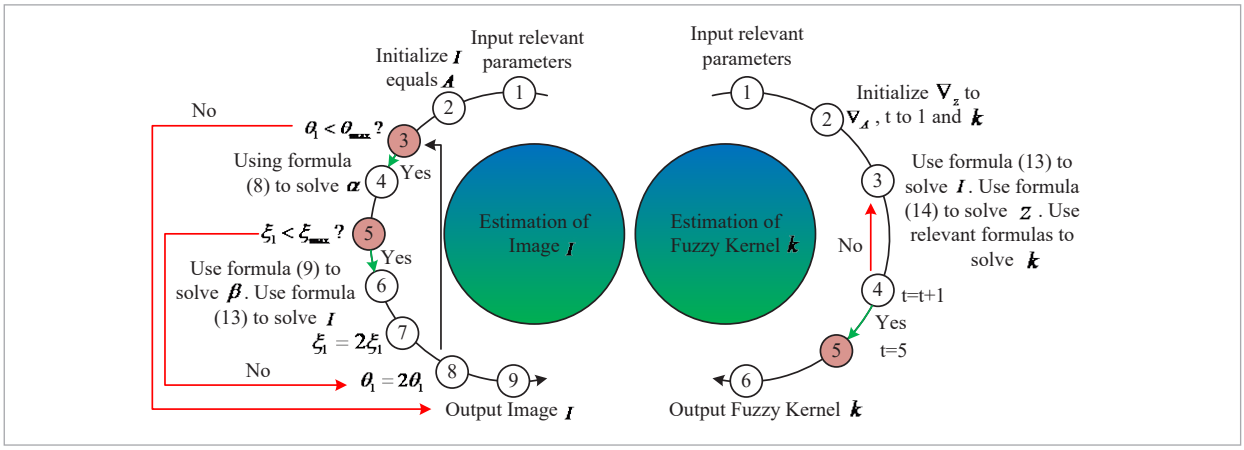

From Figure 2, for the estimation of image $I$, the relevant parameters are first inputted and $I$ is initialized to be equal to $A$. Secondly, when $\theta_1$ is less than $\theta_{max}$, Equation (8) is used to solve $\alpha$. When $\xi_1$ is less than $\xi_{max}$, equation (9) is used to solve $\beta$. Equation (13) is used to solve $I$. Next, $\xi_1$ is set to $2\xi_1$. If it is less than $\xi_{max}$, the relevant parameter is solved again. If it is not, $\theta_1$ is set to be equal to $2\theta_1$. If it is less than $\theta_{max}$, $\alpha$ is solved again and the process is repeated. If it is not, the process is ended and the image $I$ is output. When estimating the blur kernel $k$, the relevant parameters are input and $\nabla_z$ is initialized to $\nabla_A$. The index values t of the camera pose samples are 1 and $k$. Equation (13) is used to solve $I$, Equation (14) is used to solve $z$, and relevant equations are used to solve $k$. Next, t is set to t+1 until t equals 5 and the fuzzy kernel $k$ is output. In addition, the fuzzy kernel performs necessary normalization operations on negative elements after setting them to 0. It is worth noting that the study also constructs a pyramid for images, implementing fuzzy kernel estimation processing from coarse to fine. The process of this method is shown in Figure 3.

From Figure 3, the proposed DARSE-AC process first inputs a blurred color image. The input image is subjected to grayscale processing to obtain grayscale blurred images and gradient maps. Secondly, the main structure of the image is extracted, and prominent edges are depicted. Next, it is restored to a clear black and white image and the main structure of the image is extracted. Then, this process provides clear salient edges and estimates the blur kernel $k$ until a clear color image is obtained before ending the process. Otherwise, it is restored to a clear black and white image and the process is repeated. The image description of the deconvolution model and image estimation steps in this chapter is shown in Figure 4.

**Figure 3**
DARSE-AC process diagram

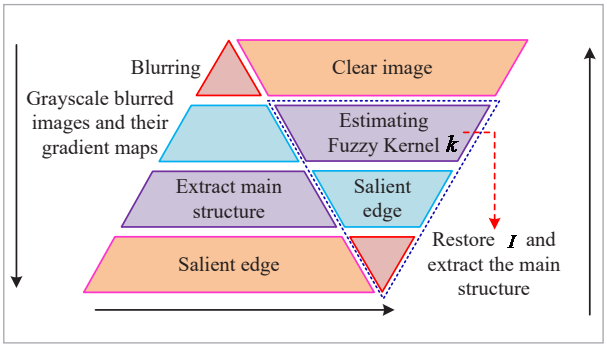


In Figure 4, when processing the image estimation, firstly, the average curvature regularization is combined with gradient and edge highlighting for image fusion. Subsequently, a new deconvolution algorithm is modeled and the equations are solved based on a hybrid segmentation strategy with the introduction of auxiliary variables. For the solution part of the equation, the mean curvature filter is used to compute the functional equation and the Fourier transform is used to obtain a closed-form solution of the equation. The fuzzy kernel in the equation is estimated using the mutual sensing image filtering method, and the calculated fuzzy kernel is subjected to the normalization operation. Finally, the construction of the image pyramid is completed.

**Figure 4**
Schematic diagram of deconvolution model and image estimation steps

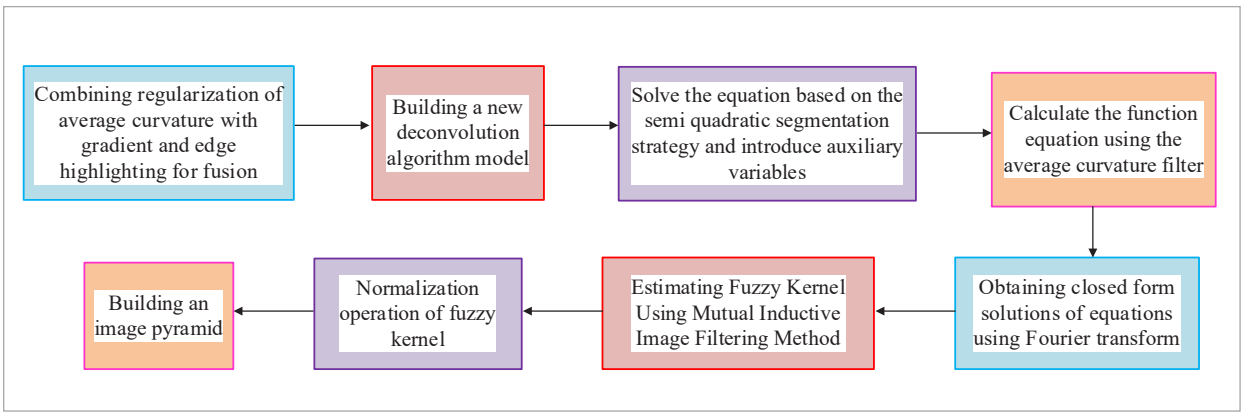

## 4. Performance Analysis of Image Deblurring Based on Darse-Ac Model

The experiment is conducted on an Intel (R) Core (TM) i5-1135G7 @ 2.40GHz 2.40GHz processor, 16.0GB of memory, Windows 10 64 bit operating system, and MATLAB 2016b operating environment. The deep learning framework is Pytorch, with the activation function parameter set to 0.2. During the training process, the image batch size is 48*48, the initial learning rate is 10, the training batch is 1000, the multi-scale layers are 4, and the number of alternating iterations for each layer of the image is set to 10. The parameters $\alpha$ and $\beta$ are 0.5 and 10, and the $\gamma$ is set to 3*103. The number of repeated experiments is 10. To verify the performance of the DARSE-AC model, a comprehensive analysis is conducted on its convergence, parameter sensitivity, effectiveness, and limitations. At the same time, it is applied to actual datasets to verify its image deblurring performance. The International Conference on Document Analysis and Recognition (ICDAR2019) text dataset, iNaturalist 2021 dataset, and low light level dataset (GLADNet) are analyzed, with approximately 1000 images. INat2021 contains over 2.7 million images from 10000 different species, each with 50 examples and 10 validation images, totaling 100000 validation images and 500000 test images. In low light environments, images often encounter problems such as blurring and noise, which pose challenges for object detection and recognition. The GLADNet dataset contains a large number of images under low light conditions, which can help researchers develop robust algorithms for low light object recognition and segmentation. The GLADNet dataset typically contains hundreds to thousands of images. The image size in the dataset (600*600) is standardized, unnecessary background parts are cropped, and contrast and brightness are adjusted to improve image quality.

### 4.1. Performance Analysis of DARSE-AC Model

Firstly, the sensitivity of the model parameters is analyzed, mainly focusing on the important parameters $\lambda$, $\xi$, $\theta$, $\tau$, and $\gamma$. The results are shown in Figure 5.

In Figure 5, parameters $\lambda$ and $\gamma$ were mainly used to explicitly select convex edges. Therefore, its reasonable range was set at $10^{-4}$. The reasonable range of parameters $\xi$ and $\theta$ was between $10^{-3}$ and $10^{-2}$. The reasonable range of parameter $\tau$ was between 1~10. From Figure 5(a), under the influence of parameters $\lambda$ and $\gamma$, the kernel similarity value was within 0.8, with little variation. Under the influence of parameters $\xi$ and $\theta$, the kernel similarity value was also within 0.8. The curve under the influence of parameter $\xi$ showed a downward trend. From Figure 5(b), the curve under the influence of parameter $\tau$ showed a more significant change compared with other parameters, but still maintained around 0.8. Overall,

**Figure 5**
Parameter sensitivity analysis results of the DARSE-AC model

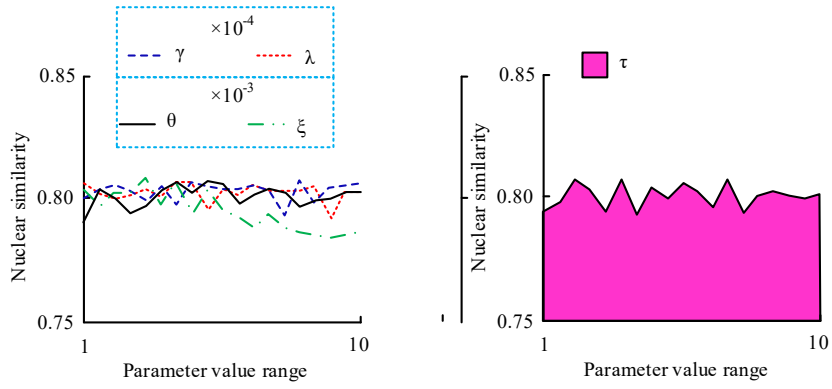


(a) Parameter λ, γ , ξ, θ impact results

(b) Parameter τ impact results

**Figure 6**
Objective function iteration curve

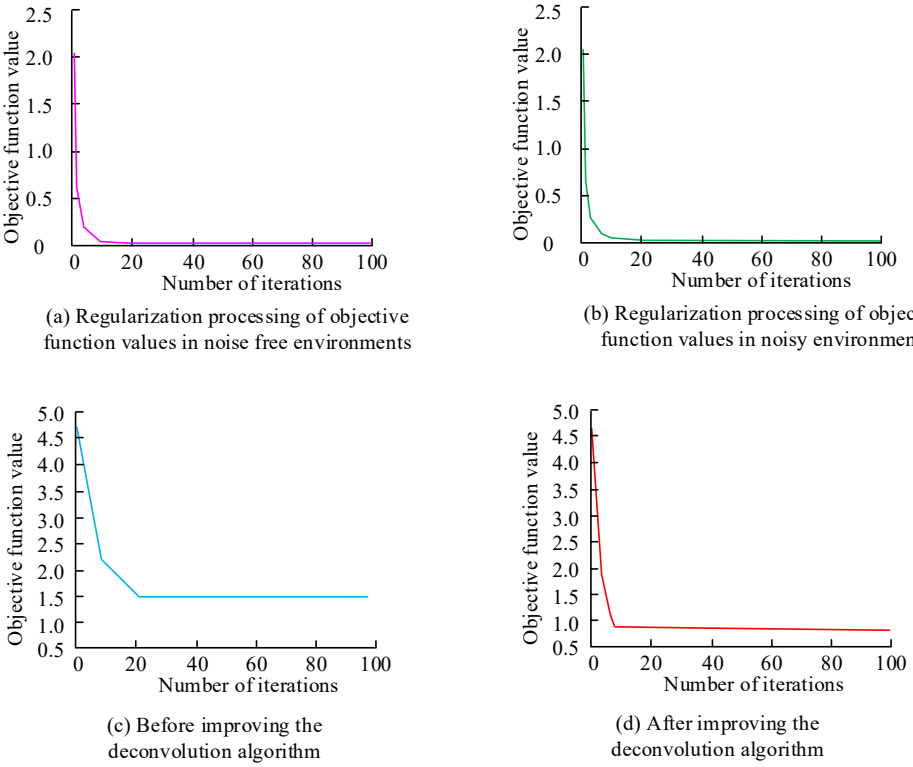


the method proposed in the study is not sensitive to changes in five important parameters. The performance analysis of the regularization improvement ideas proposed in the study is shown in Figure 6.

In Figure 6, the results indicated that the regularization improvement approach proposed in the study exhibited a more rapid iterative trend in the curve direction when solving the objective function value. Approximately after more than 10 iterations, the curve tended to converge and was less affected by the noise environment. There was a significant difference in the iteration curve of the objective function before and after the improvement of the deconvolution algorithm proposed in the study. The curve before the improvement tended to converge when the number of iterations was greater than 20, with an objective function value of 1.5, and the overall fluctuation was more obvious. The improved deconvolution algorithm had fast convergence and tended to flatten out when the number of iterations was greater than 9. The image enhancement test results under different methods are shown in Table 1.

**Table 1**
The analysis of image enhancement test results under different methods

| - | Time complexity | Actual time spent (milliseconds) | Model parameter quantity (M) |
|---|---|---|---|
| Deconvolution model | O(nlog(n) | 162 | 10.5 |
| FFT | O(m+n) | 2171 | 16.3 |

The results in Table 1 indicated that after the application of FFT, it effectively improved computational efficiency and achieve fast image enhancement. The actual application time (162 milliseconds) was significantly smaller than the model before the application (2171 milliseconds), and its model parameter count was smaller, indicating that it had good computational performance. The traditional Fourier transform method still faces computational burden when processing large-scale or high-resolution images, while the deconvolution model can directly operate in the spatial domain, avoiding complex transformations in the frequency domain and reducing time consumption. The parameters in the deconvolution model can be processed for distorted images, and automatic adjustment of parameters can reduce manual settings, so the number of parameters involved is relatively small. The quality evaluation of reconstructed images based on regularization processing is analyzed, and the results are shown in Table 2.

Table 2 showed that different algorithms had significant differences in PSNR values and SSIM values in quality processed frame results. Among them, the PSNR values for non-regularization, gradient prior, second-order generalized total variation, and single frame deconvolution methods were 18.27, 20.18, 23.44, 32.15, and SSIM values were 0.6819, 0.7334, 0.8167, and 0.8529, respectively. The values on both evaluations were smaller than the algorithm proposed in the study. The regularization modified convolution algorithm based on prominent edges and average curvature proposed in the study showed good image quality, with a SSIM value of 0.9546 between images. In image quality reconstruction, regularization and edge highlighting in the research method can effectively maintain the structural integrity and edge clarity of the image. The average curvature can effectively smooth the non-edge areas of the image, reduce artifacts, and thus improve image quality. However, the input sequence frame processing method may result in information loss due to inconsistencies between sequence frames, and non-regularization can lead to excessively smooth or noisy images. Although gradient prior and second-order generalized total variation processing can preserve image edges to a certain extent, they may not be sufficient to handle highly non-linear image distortion. Single frame deconvolution cannot guarantee the integrity of image information details. Therefore, the above comparison methods are difficult to perform well in PSNR and SSIM indicators, and it is difficult to suppress noise and balance image details. Subsequently, the evaluation results of different algorithms under different image types are analyzed, and the results are shown in Table 3.

In Table 3, the DARSE-AC model exhibited significantly better overall image quality processing performance than other algorithms in terms of information entropy, average SSIM, root mean square error, mean contrast, brightness relationship factor, and mutual information, with values of 7.442, 6.927, 1.305, 1.674, 0.924, and 8.672, respectively. The DRN algorithm performed better, and the information entropy results of VDSR algorithm and SRCNN algorithm were relatively small, with values of 7.138 and 7.171, respectively, indicating that the quality information data in their image processing is damaged. Secondly, the effectiveness of the model is analyzed. The proposed regularized convolution processing can optimize the visual quality of images by highlighting edge details and adjusting local curvature. It can achieve explicit edge selection through mutually guided image filter-

**Table 2**
Quality evaluation of reconstructed images based on regularization processing

| Algorithm | The frame with the best overall quality in the input sequence | No regular term | Deconvolution algorithm based on gradient prior | Deconvolution algorithm based on second order generalized total variations | Single frame blind deconvolution algorithm | DARSE-AC Model |
|---|---|---|---|---|---|---|
| PSNR | 3300 | 18.27 | 20.18 | 23.44 | 32.15 | 36.22 |
| SSIM | 0.9085 | 0.6819 | 0.7334 | 0.8167 | 0.8529 | 0.9546 |

**Table 3**
The analysis of image enhancement test results under different methods

| - | Information entropy | Average structural similarity | Root mean square error | Mean contrast | Brightness relationship factor (%) | Mutual information |
|---|---|---|---|---|---|---|
| VDSR [1] | 7.138 | 5.831 | 3.537 | 1.027 | 0.798 | 5.508 |
| SRCNN [31] | 7.171 | 6.271 | 3.711 | 1.231 | 0.827 | 6.574 |
| SRFBN-S [26] | 7.285 | 6.333 | 3.861 | 0.549 | 0.888 | 5.916 |
| DRN [29] | 7.196 | 6.169 | 4.129 | 0.975 | 0.901 | 6.865 |
| DARSE-AC model | 7.442 | 6.927 | 2.322 | 1.305 | 0.924 | 8.672 |

ing, which can effectively improve indicators such as information entropy, average contrast, and mutual information of images, especially when dealing with images with complex texture and edge information. Other deep convolutional neural network comparison methods (VDSR method and SRCNN method) may lack sufficient flexibility when dealing with specific types of image distortion, especially without sufficient training data. However, SRFBN-S and DRN methods are unable to achieve timely and effective image restoration for specific details, such as edge sharpening and local contrast adjustment. The indicators such as information entropy and average structural similarity mainly involve the overall feature difference information of the image. Although other comparison methods are slightly less efficient and effective than the proposed method, there is not a significant difference in their overall grasp of image quality. Mutual information measures the statistical correlation between two images, which is an important measure of image similarity. The significant deviation of the DARSE-AC model from other methods in this metric may be due to its particular emphasis on handling edges and local curvature. Compared with methods based on deep learning, it may exhibit greater variability in specific image content, especially when the information distribution in the image is extremely uneven and less affected by image noise and details. ICDAR2019 text dataset (set as datasets M and I) is selected for the experiment. Ablation experiments are conducted on two datasets. The parameter $\lambda$ is 0, and the $\theta$ is 0. Mutual guidance image filtering is replaced by impulse filtering and research method, set to A~E, respectively. The results are shown in Figure 7.

**Figure 7**
Results of ablation experiments on the research method

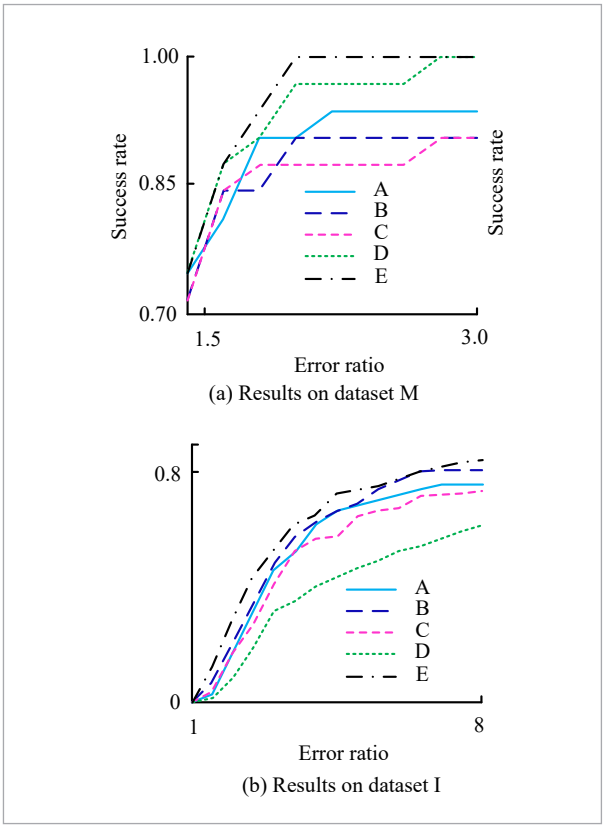


From Figure 7(a), as the ER increased, the success rate of image denoising for all five methods showed a stepwise increase. The highest success rate of method A was 93.5%. The methods B and C were 90%. The highest success rate for methods D and E was 100%.

Method E reached its highest value when the ER was 2. Method D reached its highest value at an ER of 2.75. From Figure 7(b), as the ER increased, the success rate of image denoising for all five methods showed a smooth growth. The success rate of the research method was higher than that of comparative methods, reaching a maximum of 81.2%. Overall, both explicit edge selection and AC regularization can effectively improve the image denoising effect. The research method combines these two modules to achieve the best performance in different combinations. To visualize the contribution of each module, a restoration image of a randomly selected blurred image in the ICDAR2019 text dataset is analyzed separately. The results are shown in Figure 8.

Figure 8 shows the processing result of the blurred image. From Figure 8(a), the restoration results were not ideal when the parameter $\lambda$ was 0. The restoration results tended to deteriorate. The restoration results were improved compared with $\lambda$ was 0 when the parameter $\theta$ was 0. Some fonts could be seen clearly, but there were still blurry fields. The DARSE-AC model with convex edges and AC regularization has higher deblurring effect and effectiveness. In Figure 8(b), parameter $\lambda$ was 0, which essentially indicated that there was no significant edge extraction in the intermediate results. The parameter $\theta$ was 0, which essentially showed that there was no AC regularization in the intermediate result. The research method included these two modules. From Figure 8(b), when parameter $\lambda$ was 0, the restoration process initially tended to clearer. Some fonts could be seen clearly, but the final result became increasingly blurry. When parameter $\theta$ was 0, the restoration results showed the same trend, the image blurring under the influence of the research method continuously decreased, ultimately showing clear results. From Figure 8(a)-(b), the DARSE-AC model with salient edges and AC regularization has higher deblurring effect and effectiveness.

Finally, the convergence and limitations of the model are analyzed. In the convergence analysis of the DARSE-AC model, the iterations are 50. The convergence is verified from two aspects: the change in average energy function value and the change in average kernel similarity. In the limitation verification, the

**Figure 8**
Image blur processing results


(a) Comparison of fuzzy image restoration results in text dataset


(b) Comparison of algorithms for fuzzy image restoration

**Figure 9**
Convergence analysis results of DARSE-AC model

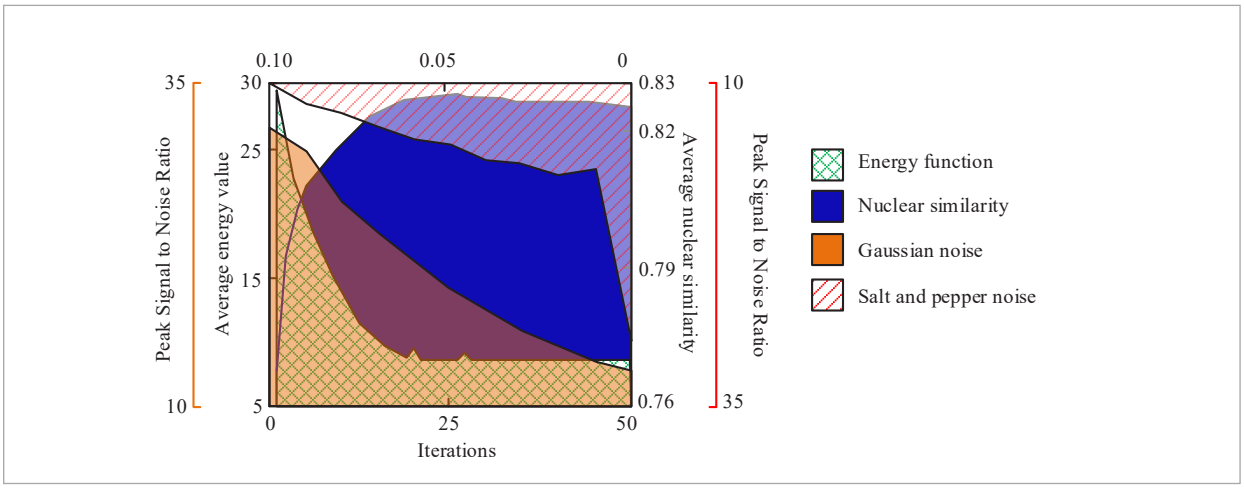


research method on blurred images with Gaussian noise level and salt and pepper noise level are evaluated. The evaluation index is PSNR. The results are shown in Figure 9.

In Figure 9(a), as the number of iterations increased, the average energy function value continued to decrease. After approximately 18 iterations, it reached 8 and stabilized. It fluctuated between 20 and 27 iterations, but overall remained stable. The reason for fluctuations is that the selection of penalty parameters during image deblurring can affect the convergence speed and stability of the algorithm. Calculating the surface curvature of the image based on the curvature of each pixel in the approximate image domain can lead to certain errors. As the number of iterations increases, the average kernel similarity value continues to increase. In Figure 9(b), the increase in noise led to a continuous decrease in the PSNR of the research method, which affected the overall performance. Overall, DARSE-AC shows regional stability and some convergence in 50 iterations, but it still needs improvement when dealing with blurry images with severe noise.

## 4.2. Actual Deblurring Performance Analysis of DARSE-AC Model

To further verify the deblurring performance of the DARSE-AC model, the study validates it on the iNaturalist 2021 dataset and the low light dataset (GLAD-Net). When conducting quantitative comparisons on the iNaturalist 2021 dataset, fast motion deblurring method, two-stage kernel estimation deblurring method, normalized blind deconvolution deblurring method, and significant kernel estimation deblurring method (represented by 1-4) are introduced. The edge fuzzy kernel estimation, extreme channel prior deblurring method, depth discrimination prior deblurring method, and surface perception deblurring method (represented by 5-8) are analyzed. The specific content of the comparison method is shown in Table 4.

They were compared with the DARSE-AC model. The hyper-parameters $\lambda$, $\xi$, $\theta$, $\tau$ and $\gamma$ are set as 4e-4, 4e-3, 4e-3, 2, and 8e-4 respectively in the experiment. The experimental environment is matrix laboratory. The quantitative results are shown in Table 5.

In Table 5, O, P, Q, and R represent the evaluation metrics PSNR, Structure Similarity Index Measure (SSIM), ER, and success rate, respectively. From Table 4, the PSNR, SSIM, and ER values of the DARSE-AC model were 31.03, 0.96, and 1.61, respectively, which were higher than comparative methods. The success rate was as high as 99.54%, significantly better than comparative methods. Overall, the research method has the best deblurring performance on the iNaturalist 2021 dataset. To further validate the superiority of the research method, different methods are compared for PSNR and SSIM values on the GLAD-Net dataset and the ICDAR2019 dataset. The success rates of different methods under different ERs are shown in Figure 10.

**Table 4**
Comparison Methods on iNaturalist 2021 Dataset

| Serial number | Method | Design concept | Reference |
|---|---|---|---|
| 1 | Fast motion deblurring method | Using local fuzzy perception gating network and fuzzy perception patch pruning strategy to locate fuzzy regions in local motion blur dataset. | [16] |
| 2 | Two-stage kernel estimation deblurring method | Implementing motion image deblurring using a two-stage convolutional neural network (CNN) to jointly learn the U-Net architecture strategy. | [22] |
| 3 | Normalized blind deconvolution deblurring method | Developed a benchmark for validating non blind deconvolution methods. | [3] |
| 4 | Significant kernel estimation deblurring method | Propose a fractional order (spatial and temporal) total variation regularization model to improve model efficiency through fuzzy membership degrees with regular changes. | [14] |
| 5 | Edge fuzzy kernel estimation | Propose a blind image restoration method combining fuzzy kernel estimation and CNN, and use fuzzy support parameter estimation to achieve automatic feature line detection. | [11] |
| 6 | Extreme channel prior deblurring method | Using specific region priors and image deblurring techniques to enhance the true edges of images. | [23] |
| 7 | Depth discrimination prior deblurring method | Designed a dual fusion neural network consisting of a deep generative network and a discriminative network. | [6] |
| 8 | Surface perception deblurring method | Restoration of Blurred Images Using Modified Fuzzy Generative Adversarial Networks. | [4] |

**Table 4**
Comparison results of indicator performance among different methods on the same dataset

| - | 1 | 2 | 3 | 4 | 5 |
|---|---|---|---|---|---|
| PSNR | 26.22 | 28.29 | 23.20 | 23.91 | 29.51 |
| SSIM | 0.87 | 0.92 | 0.81 | 0.83 | 0.93 |
| ER | 8.69 | 3.62 | 11.64 | 9.19 | 2.36 |
| Success rate (%) | 78.90 | 94.98 | 67.13 | 68.67 | 97.32 |
| - | 6 | 7 | 8 | DARSE-AC | |
| PSNR | 30.82 | 30.67 | 30.72 | 31.03 | |
| SSIM | 0.94 | 0.94 | 0.94 | 0.96 | - |
| ER | 1.70 | 1.82 | 1.82 | 1.61 | |
| Success rate (%) | 98.34 | 98.34 | 98.22 | 99.54 | |

In Figure 10, the blur kernel size is set to 51×51. The same non-blind deblurring algorithm is used to obtain the final clear image (using the non-blind deblurring algorithm of natural image blocks). In Figure 10 (a), an increase in ER value led to an increase in the success rate of deblurring for different methods, with Method 1 and Method 2 having relatively faster growth rates. The highest success rate of Method 1 was about 78%. Method 2 achieved a maximum value of approximately 95%. In Figure 10 (b), the research method reached the highest value, about 99%, with an error rate of about 4 compared with other methods.

Figure 11 shows a comparison of PSNR and SSIM values using different methods on the GLADNet dataset and ICDAR2019 dataset.

**Figure 10**
Comparison of success rates of different methods under different ERs

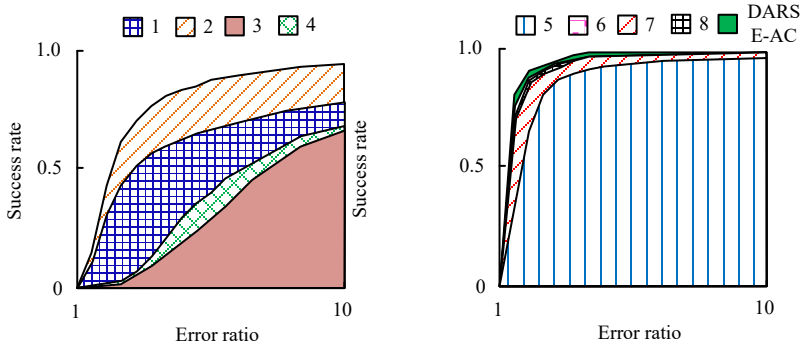


(a) The success rates of methods 1-4 under different ER conditions

(b) The success rates of methods 5-8 and research methods under different ER conditions

In Figure 11, methods 5 and 8 were not suitable for these two datasets, so they were removed. A deblurring method using L0 normal form combined with regularization is synchronously introduced, namely Equation (9). From Figure 11(a), the PSNR value of the research method in dataset ICDAR2019 was 30.29, and the SSIM value was 0.96, both higher than comparative methods. From Figure 11(b), the PSNR value of the research method in the dataset GLADNet was 25.16, and the SSIM value was 0.90, which was also higher than comparative methods. Overall, in the quantitative comparison between the two datasets, the research method shows the best performance, indicating that the research method has higher applicability and generalization ability. To further validate the performance of the DARSE-AC model, images are randomly selected on the dataset GLADNet to compare the deblurring visual effects of different methods. A more challenging Realistic Single Image Dehazing (RESID) dataset is introduced to validate the performance.

**Figure 11**
Comparison of PSNR and SSIM values using different methods on the GLADNet and ICDAR2019 datasets

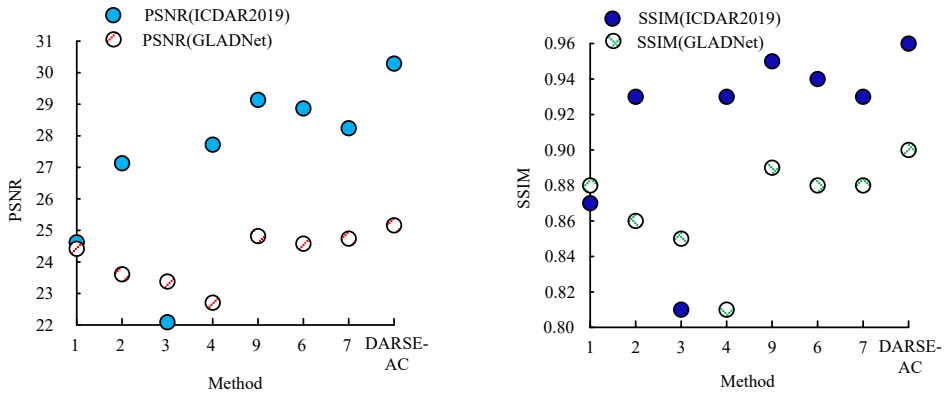


(a) PSNR value results of different methods on two datasets

(b) SSIM value results of different methods on two datasets

Among them, Method 1 and Method 4 are selected as comparative methods on the dataset GLADNet. The results of removing blurred low light images using different methods are shown in Figure 12.

From Figures 12(c)-(d), methods 1 and 2 improved clarity compared with the original blurred image, i.e. Figure 12(a). However, compared with the original clear image and blur kernel, there still existed blurriness. From Figure 12(e), the research method achieved the best results among the three methods. The actual restoration results show that generated images are clearer and have less residual blur, which are closer to Figure 12(b).

On this basis, different methods are compared for true fuzziness in the dataset RESID through random screening. The visual effect of the restoration results on low light images is shown in Figure 13.

In Figure 13, to avoid repetition, methods 3 and 9 were selected for comparison. They used the same non-blind deconvolution algorithm to achieve better visualization (using the non-linear non blind deconvolution algorithm of light fringes). From Figure 13(a), the original blurred image of the license plate number and the locally enlarged image were completely unclear. From Figure 13(b), method 3 improved the image clarity, but there was still noise and blurred lines. From Figure 13(c), method 9 improved compared with method 3, but there was still ambiguity. From Figure 13(d), the fuzzy kernel of the research method contained less noise. The restored image had better visual quality. The DARSE-AC model has better performance and stronger image restoration ability on different datasets. Finally, the study compares the average PNSR quantitative evaluation results of different methods in the dataset RESID, as shown in Table 6.

In Table 6, the study screened five types (represented by e~i) from the RESID dataset, including artificial images, natural images, humans, saturated solutions, and text. From Table 5, the research method had advantages in the PSNR values for artificial and natural images in the dataset RESID, with values of 19.24 and 23.61, respectively. Method 7 had advantages in humans, saturated solutions, and texts, with values of 25.77, 16.61, and 17.98, respectively. Overall, the PNSR value of DARSE-AC was 20.56, which was superior to comparative methods, indicating its superiority.

**Figure 12**

Comparison results of different methods for removing blurry low light images

(a) Blur Image (b) Clear Image and Blur Kernel (c) Method 1 (d) Method 2 (e) DARSE-AC

**Figure 13**

Visual effects of different methods on restoration results of realistic blurred low light images in the RESID dataset


(a) Blur Image (b) Method 3 (c) Method 9 (d) DARSE-AC

**Table 6**
Average PNSR quantitative results demonstrated by different methods

| - | 1 | 2 | 3 | 4 | 9 | 6 | 7 | 8 | DARSE-AC |
|---|---|---|---|---|---|---|---|---|---|
| e | 16.34 | 19.21 | 15.72 | 15.05 | 16.91 | 18.31 | 18.84 | 18.76 | 19.24 |
| f | 20.12 | 13.01 | 19.42 | 20.05 | 20.90 | 22.96 | 23.35 | 23.11 | 23.61 |
| g | 19.88 | 25.30 | 21.48 | 20.34 | 23.34 | 25.70 | 25.77 | 25.53 | 25.37 |
| h | 14.04 | 14.78 | 14.07 | 15.34 | 14.60 | 16.56 | 16.61 | 16.52 | 16.50 |
| i | 14.85 | 18.54 | 15.39 | 14.88 | 16.85 | 17.64 | 17.98 | 17.68 | 17.96 |
| Total | 17.05 | 20.17 | 17.22 | 17.14 | 18.52 | 20.24 | 20.51 | 20.32 | 20.56 |

## 5. Conclusions

At present, in the actual imaging process of visual communication, many factors lead to image blurring and high noise. This study combined convex edges with AC regularization to propose DARSE-AC. The effectiveness was verified. From the experimental results, in the parameter sensitivity analysis, the values of the five parameters remained around 0.8, indicating that the parameter sensitivity of the research method was not high. As the error rate increased, the success rate of deblurring for all five methods showed a gradually increasing trend. The highest success rate of method A was 93.5%. The highest success rate of methods B and C was 90%. The highest success rate of methods D and E was 100%. In addition, the PSNR, SSIM, and ER values of the DARSE-AC model were 31.03, 0.96, and 1.61, respectively, with a success rate of 99.54%, which was higher than comparative methods. The research method generated clearer images with less residual blur. Meanwhile, the overall PNSR value of the research method in the RESID dataset was 20.56, which was better than comparative methods. Based on the current research status of poor image deblurring quality, this paper designs an improved algorithm based on regularization and deconvolution, highlighting edges and average curvature. Regularization processing can overcome the disadvantages of geometric features that cannot be saved, high computational costs, and difficult parameter selection in image restoration methods. After improving the model to a spatially adaptive mixed variation model, the design of spatially adaptive parameters can suppress noise, highlight edges, and improve smoothness. The salient edge selection method can remove noise and texture from intermediate images while preserving salient edges, which is beneficial for fuzzy kernel estimation. Calculating the curvature of an image surface by approximating each pixel in the image domain inevitably leads to certain errors. Therefore, in future research, it is necessary to more accurately find the tangent planes of the center point in different directions and calculate the arc length between the center point and adjacent points to reduce errors. However, in actual imaging, blur degradation is mostly spatially variable, and existing spatially variable degradation models still cannot well describe the real degradation process. Therefore, establishing a realistic and effective fuzzy degradation model is one of the key focuses of future work.

## Reference

1. Ayas, S., Ekinci, M. Microscopic Image Super-Resolution Using Deep Convolutional Neural Networks. Multimedia Tools and Applications, 2020, 79(21-22), 15397-15415. https://doi.org/10.1117/1.JBO.28.3.036501
2. Baldwin, R. W., Liu, R., Almatrafi, M., Asari, V., Hirakawa, K. Time-Ordered Recent Event (TORE) Volumes for Event Cameras. IEEE Transactions on Pattern Analysis and Machine Intelligence, 2023, 45(2), 2519-2532. https://doi.org/10.1109/TPAMI.2022.3172212
3. Chaganova, O. B., Grigoryev, A. S., Nikolaev, D. P., Nikolaev, I. P. Applied Aspects of Modern Non-Blind Image Deconvolution Methods. Компьютерная Оптика, 2024, 48(4), 562-572. https://doi.org/10.18287/2412-6179-CO-1409

4. Choi, J., Hong, J. S., Owais, M., Kim, S. G., Park, K. R. Restoration of Motion Blurred Image by Modified DeblurGAN for Enhancing the Accuracies of Finger-Vein Recognition. Sensors, 2021, 21(14), 4635. https://doi.org/10.3390/s21144635
5. oeurjolly, D., Lachaud, J. O., Gueth, P. Digital Surface Regularization with Guarantees. IEEE Transactions on Visualization and Computer Graphics, 2021, 27(6), 2896-2907. https://doi.org/10.1109/TVCG.2021.3055242
6. Cui, Z. P. Restoration and Enhancement of Fuzzy Defect Image Based on Neural Network. Journal of Computer Education, 2023, 34(4), 1-14. https://doi.org/10.53106/199115992023083404001
7. Fairag, F., Chen, K., Brito-Loeza, C., Ahmad, S. A Two-Level Method for Image Denoising and Image Deblurring Models Using Mean Curvature Regularization. International Journal of Computer Mathematics, 2022, 99(4), 693-713. https://doi.org/10.1080/00207160.2021.1929939
8. Fatichah, C., Amaliah, B. Image Enhancement Using Deblur Generative Network and Deep Deblur Adversarial. Proceedings of IEEE International Conference on Industry 4.0, IAICT, 2024, 136-141. https://doi.org/10.1109/IAICT62357.2024.10617633
9. Gampala, V., Kumar, M. S., Sushama, C., Raj, E. F. I. Deep Learning-Based Image Processing Approaches for Image Deblurring. Materials Today: Proceedings, 2020, 10 (Dec). https://doi.org/10.1016/j.matpr.2020.11.076
10. Hasanvand, M., Nooshyar, M., Moharamkhani, E., Selyari, A. Machine Learning Methodology for Identifying Vehicles Using Image Processing. Artificial Intelligence Applications, 2023, 1(3), 170-178. https://doi.org/10.47852/bonviewAIA3202833
11. Huang, L., Xia, Y. Joint Blur Kernel Estimation and CNN for Blind Image Restoration. Neurocomputing, 2020, 396, 324-345. https://doi.org/10.1016/j.neucom.2018.12.083
12. Imani, M. A Random Patches-Based Edge Preserving Network for Land Cover Classification Using Polarimetric Synthetic Aperture Radar Images. International Journal of Remote Sensing, 2021, 42(13), 4942-4960. https://doi.org/10.1080/01431161.2021.1906984
13. Jing, W., Jin, T., Xiang, D. SAR Image Edge Detection with Recurrent Guidance Filter. IEEE Geoscience and Remote Sensing Letters, 2021, 18(6), 1064-1068. https://doi.org/10.1109/LGRS.2020.2990688
14. Khan, M. A., Ullah, A., Khan, S., Ali, M., Khan, S., Khan, K., Masud, M., Ali, J. A Novel Fractional-Order Variational Approach for Image Restoration Based on Fuzzy Membership Degrees. IEEE Access, 2021, 9, 43574-43600. https://doi.org/10.1109/ACCESS.2021.3066127
15. Kumawat, A., Panda, S. A Robust Edge Detection Algorithm Based on Feature-Based Image Registration (FBIR) Using Improved Canny with Fuzzy Logic (ICWFL). Visual Computing, 2022, 38(11), 3681-3702. https://doi.org/10.1007/s00371-021-02196-1
16. Li, H., Zhang, Z., Jiang, T., Luo, P., Feng, H., Xu, Z. Real-World Deep Local Motion Deblurring. Proceedings of the AAAI Conference on Artificial Intelligence, 2023, 37(1), 1314-1322. https://doi.org/10.1609/aaai.v37i1.25215
17. Liu, H., Tai, X. C., Kimmel, R., Glowinski, R. A Color Elastica Model for Vector-Valued Image Regularization. SIAM Journal on Imaging Sciences, 2021, 14(2), 717-748. https://doi.org/10.1137/20M1354532
18. Liu, J., Ren, Z., Chen, Z., Liang, Y. A Multi-Frame Blind Deconvolution Algorithm with the Consistency Constraints. SPIE, 2020, 11455, 816-821. https://doi.org/10.1117/12.2564488
19. Liu, J., Shang, J., Liu, R., Fan, X. Attention-Guided Global-Local Adversarial Learning for Detail-Preserving Multi-Exposure Image Fusion. IEEE Transactions on Circuits and Systems for Video Technology, 2022, 32(8), 5026-5040. https://doi.org/10.1109/TCSVT.2022.3144455
20. Liu, J., Tan, J., He, L. A Fast Blind Image Deblurring Method Using Salience Map and Gradient Cepstrum. Visual Computing, 2023, 39(7), 3091-3107. https://doi.org/10.1007/s00371-022-02515-0
21. Liu, X., Yang, J., Zou, C., Chen, Q., Yan, X., Chen, Y., Cai, C. Collaborative Edge Computing With FPGA-Based CNN Accelerators for Energy-Efficient and Time-Aware Face Tracking System. IEEE Transactions on Computational Social Systems, 2022, 9(1), 252-266. https://doi.org/10.1109/TCSS.2021.3059318
22. Lu, Y. C., Liu, T. P., Lin, C. H. Two-Stage Single Image Deblurring Network Based on Deblur Kernel Estimation. Multimedia Tools and Applications, 2023, 82(11), 17055-17074. https://doi.org/10.1007/s11042-022-14116-z
23. Pooja, S., Mallikarjunaswamy, S., Sharmila, N. Image Region Driven Prior Selection for Image Deblurring. Multimedia Tools and Applications, 2023, 82(16), 24181-24202. https://doi.org/10.1007/s11042-023-14335-y
24. Priya, S., Letitia, S. Exponential-Ant Cuckoo Search Optimization for Image Deblurring with Spinal Cord Images Based on Kernel Estimation. Signal, Image and Video Processing, 2022, 16(2), 339-347. https://doi.org/10.1007/s11760-021-01929-y

25. Rajora, S., Butola, M., Khare, K. Regularization-Parameter-Free Optimization Approach for Image Deconvolution. Applied Optics, 2021, 60(19), 5669-5677. https://doi.org/10.1364/AO.426353

26. Sahito, F., Zhiwen, P., Sahito, F., Ahmed, J. Transpose Convolution-Based Model for Super-Resolution Image Reconstruction. Applied Intelligence, 2023, 53(9), 10574-10584. https://doi.org/10.1007/s10489-022-03745-4

27. Steeden, J. A., Quail, M., Gotschy, A., Mortensen, K. H., Hauptmann, A., Arridge, S., Muthurangu, V. Rapid Whole-Heart CMR With Single Volume Super-Resolution. Journal of Cardiovascular Magnetic Resonance, 2020, 22(1), 1-13. https://doi.org/10.1186/s12968-020-00651-x

28. Syed, M. H., Upreti, K., Nasir, M. S., Alam, M. S., Sharma, A. K. Addressing Image and Poisson Noise Deconvolution Problem Using Deep Learning Approaches. Computational Intelligence, 2023, 39(4), 577-591. https://doi.org/10.1111/coin.12510

29. Wang, B., Liu, C., Yan, B., Yang, X. Lightweight Parallel Feedback Network for Image Super-Resolution. Neural Processing Letters, 2023, 55(3), 3225-3243. https://doi.org/10.1007/s11063-022-11007-0

30. Wang, C., Zhang, Z., Guo, Z., Zeng, T., Duan, Y. Efficient SAV Algorithms for Curvature Minimization Problems. IEEE Transactions on Circuits and Systems for Video Technology, 2023, 33(4), 1624-1642. https://doi.org/10.1109/TCSVT.2022.3217586

31. Wu, J., Bai, T., Li, X. Inverting Chlorophyll Content in Jujube Leaves Using a Back-Propagation Neural Network-Random Forest-Ridge Regression Algorithm with Combined Hyperspectral Data and Image Color Channels. Agronomy, 2024, 14(1), 140. https://doi.org/10.3390/agronomy14010140

32. Wu, J., Ma, J., Liang, F., Dong, W., Shi, G., Lin, W. End-to-End Blind Image Quality Prediction with Cascaded Deep Neural Network. IEEE Transactions on Image Processing, 2020, 29, 7414-7426. https://doi.org/10.1109/TIP.2020.3002478

33. Xie, J., Hou, G., Wang, G., Pan, Z. A Variational Framework for Underwater Image Dehazing and Deblurring. IEEE Transactions on Circuits and Systems for Video Technology, 2022, 32(6), 3514-3526. https://doi.org/10.1109/TCSVT.2021.3115791

34. Xu, C., Wang, J., Tao, J., Zhang, J., Zhong, R. Y. A Knowledge-Augmented Image Deblurring Method with Deep Learning for In-Situ Quality Detection of Yarn Production. International Journal of Production Research, 2023, 61(13), 4220-4236. https://doi.org/10.1080/00207543.2021.2010827

35. Yang, Y., Liu, J., Huang, S., Wan, W., Wen, W., Guan, J. Infrared and Visible Image Fusion via Texture Conditional Generative Adversarial Network. IEEE Transactions on Circuits and Systems for Video Technology, 2021, 31(12), 4771-4783. https://doi.org/10.1109/TCSVT.2021.3054584

36. Yin, F., Li, C., Wang, H., Zhou, S., Nie, L., Zhang, Y., Yin, H. A Robust Denoised Algorithm Based on Hessian-Sparse Deconvolution for Passive Underwater Acoustic Detection. Journal of Marine Science and Engineering, 2023, 11(10). https://doi.org/10.3390/jmse11102028

37. Yogananda, G. S., Babu, J. A. Multiobjective Reptile Search Algorithm-Based Effective Image Deblurring and Restoration. Journal of Artificial Intelligence Technologies, 2023, 3(4), 154-161. https://doi.org/10.37965/jait.2023.0204

38. Zhang, J., Pan, J., Wang, D., Zhou, S., Wei, X., Zhao, F., Ren, J. J. Deep Dynamic Scene Deblurring from Optical Flow. IEEE Transactions on Circuits and Systems for Video Technology, 2022, 32(12), 8250-8260. https://doi.org/10.1109/TCSVT.2021.3084616